# Decoding the Pair Distribution Function of Uranium in Molten Fluoride Salts from X-Ray Absorption Spectroscopy Data by Machine Learning

Kaifeng Zheng, Nicholas Marcella, Anna L. Smith, and Anatoly I. Frenkel*

Cite This: https://doi.org/10.1021/acs.jpcc.4c01898

Read Online

ACCESS | Metrics & More | Article Recommendations | SI Supporting Information

**ABSTRACT:** Thermal properties of actinides in molten salts are linked to the strongly disordered local environment of actinide ions. We illustrate both the limitations of the commonly used fitting method for analysis of extended X-ray absorption fine structure (EXAFS) spectra in molten $UF_4$ and a possible solution using an "objective neural network-EXAFS" (ONNE) method. ONNE provides both extraction of the pair distribution function, as validated by its application to the EXAFS spectra calculated on molecular dynamics trajectory, and the EXAFS data reconstruction. The ONNE analysis of the molten $UF_4$ has revealed reduction of the first nearest neighbor U−F coordination number, expansion of the U−F bond length, and smaller contribution to the second shell compared to current molecular dynamics models. This method is therefore an attractive alternative to conventional EXAFS analysis and molecular dynamics simulations for studies of disordered environment of actinides in molten salts.
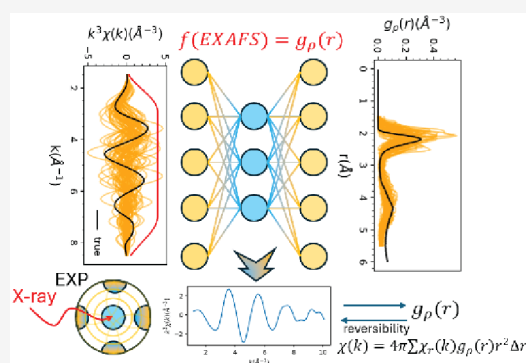
## INTRODUCTION

Unlocking the details of the local atomic environment in functional materials is critical to understanding their physical and chemical properties and gaining mechanistic insights. For example, subtle changes in the bonding environment within the first coordination shell of Ge in phase change materials may result in crystallization or amorphization, leading to changes in their optical properties.[1] Other examples include catalysts,[2−12] electrocatalysts,[13] battery,[14,15] and fuel cell[16] materials, in which the local environment of the active sites may change in reaction conditions, directly affecting their activity, selectivity, and/or stability. While numerous examples exist where the local structure−property relationship has been deciphered, their success on a case-by-case basis also illustrates the key challenge: extracting detailed information about the local structure of the active sites is often ambiguous and error-prone in materials with heterogeneously distributed active species and sites.

These challenges are further amplified when considering the paucity of experimental tools, e.g., X-ray diffraction and electron microscopy, for probing the local coordination environments. Furthermore, a workhorse method of structural analysis of disordered materials, extended X-ray absorption fine structure (EXAFS) spectroscopy, is still limited in its ability to extract structure characteristics of the local environment of X-ray absorbing atoms (i.e., coordination numbers, distances, and mean squared relative disorder) in the presence of hetero-geneity.[17] This challenge is particularly evident in disordered

systems like ionic liquids or molten salts, where co-existing coordination states of metal ions defy reliable analysis by EXAFS; commonly used fitting methods in these cases tend to underestimate coordination numbers and bond length disorder, underscoring the need for advanced methodologies that account for the complexity of these environments.[18]

Among the possible solutions, the most commonly used is the "forward" modeling of EXAFS data, wherein the atomic environment is first analyzed theoretically, using semi-empiric or first-principles molecular dynamics (MD) simulations.[19−23] Subsequently, EXAFS is calculated at each time step and averaged over the MD trajectory to compare it with the experimental EXAFS spectrum. Good agreement between MD-simulated EXAFS (MD-EXAFS) and experimental EXAFS validates the model used in MD simulations, providing all of the needed information about the structure and dynamics of the metal ion environment. With a clear advantage over conventional EXAFS analysis methods, the MD-EXAFS method has an important and obvious limitation: its model dependence.[24] It is also unclear how to handle disagreements between MD-EXAFS and the experiment.

One example of such challenge is the case of molten $UF_4$,[19] an important material for the energy industry, because it belongs to a large class of molten salts that are promising for molten salt nuclear reactors (MSRs) as coolants and liquid fuels.[25] The non-ideality and complexity at high temperatures of the irradiated molten salt system under MSR operating conditions are key reasons why their underlying behaviors in working conditions should be fundamentally understood. This knowledge is essential to be able to build predictive models for multi-component molten salt systems that can be reliably used for a thorough safety assessment during operation and accidental conditions. To uncover those behaviors, understanding the local structure of the actinide ion, such as the details of the coordination environment and chemical speciation (i.e., formation of a dissociated ionic liquid, of molecular complexes, or polymerization) at the high temperatures, is crucial. Although there are many reports investigating the local structure of different molten salt systems using spectroscopy and scattering techniques, such as X-ray/neutron diffraction,[26−30] Raman spectroscopy,[31−35] and EXAFS,[36−40] the interpretation of the data is very limited due to the strongly disordered nature of these materials that contain multiple co-existing coordination states.[22,40] The local structure of molten $UF_4$ and its mixtures with other alkali halides was studied by the MD-EXAFS method;[41−43] however, the predicted EXAFS spectra from MD simulations often showed significant discrepancies with the experimental data.

One direction that can offer a solution to this problem is the use of an "inverse" modeling approach, such as Reverse Monte Carlo (RMC),[44−50] regularization method,[51−55] and one enabled by the application of supervised machine learning methods.[56,57] Recently, a method of extracting the pair distribution function $(g_\rho(r))$ around an X-ray absorbing atom from an EXAFS spectrum was developed.[58,59] However, the theoretical training set for the artificial neural network (NN) that maps EXAFS on $g_\rho(r)$ was constructed using MD-EXAFS; hence, the resultant $g_\rho(r)$ function extracted using the neural network approach was model-dependent. A recently developed follow-up method, utilizing an "objective" training approach,[24] was shown to provide reliable results for Ni complexes in molten salt mixtures, and thus is a good starting point for extending this method to the molten actinide salt research. In the remainder of this article, we demonstrate the use of the latter method for the case of uranium EXAFS data in molten $UF_4$. The method extends naturally to the task of comparing local environments around U in $UF_4$ mixtures with other salts, to other uranium halides and their mixtures, and to other actinide-containing salts.

## METHODS

**Traditional EXAFS Analysis.** Commonly used, fitting-based, EXAFS analysis encodes the unknown local structure of the atomic environment based on the concept of photoelectron scattering paths that, in the case of single-scattering paths (corresponding to the coordination shells around the X-ray absorbing atoms), allows the determination of three characteristics of each coordination shell: coordination number ($N$), bond length ($R$), and Debye−Waller factor ($\sigma^2$) explicitly listed in the EXAFS equation:

$$\chi(k) = \sum_j \frac{N_j S_o^2}{k R_j^2} f_i(k) e^{-2k^2 \sigma_j^2} e^{-2R_j/\lambda} \sin(2kR_j + \delta_j(k)) \tag{1}$$

where $k$ is the photoelectron wavenumber, and $S_0^2$ is the passive electron reduction factor. In addition, the types of neighbors to each absorbing atom can be discerned based on the differences in their photoelectron scattering functions, $f(k)$, $\delta(k)$, and $\lambda(k)$. The summation is performed over all paths $j$, and the multiple-scattering paths are also represented by the same terms in eq 1, where the meaning of the bond length is generalized to the "half-path length." This equation relies on the assumption that the bond length disorder in the material is Gaussian or quasi-Gaussian. Using eq 1, the unknown structural variables ($N$, $R$, $\sigma^2$) are determined from the nonlinear least-squares fitting of the EXAFS equation to the experimental spectra. The assumption of Gaussian or quasi-Gaussian bond length disorder notably fails in the case of metal complexes in pure and mixed molten salts.[22,40]

**Molecular Dynamics (MD)-EXAFS.** The MD-EXAFS method offers a significant improvement over the traditional fitting method. The EXAFS spectrum is calculated for a series of extracted MD trajectories, whereby a very large number of atomic configurations (typically 25 000) are averaged, so as to reproduce the effect of the Debye−Waller factor and anharmonic vibrations, and compared to the experimental EXAFS. Based on MD trajectory, one can explicitly study the local structure: the short-range order and medium-range order of selected atoms using the pair distribution function $(g_\rho(r))$, which can be used to define the time- and configuration-average EXAFS spectrum and the coordination number and the distance over a given shell (with thickness $\Delta r$):

$$\chi(k) = 4\pi \sum_{r_{min}}^{r_{max}} \chi(k, r_i) g_\rho(r_i) r_i^2 \Delta r \tag{2}$$

$$g_\rho(r_i) = \frac{dN}{4\pi r_i^2 dr} \approx \frac{\Delta N}{4\pi r_i^2 \Delta r} \tag{3}$$

$$f(r_i) = 4\pi g_\rho(r_i) r_i^2 \Delta r \tag{4}$$

$$N_{shell} = \int_{r1}^{r2} f(r_i) dr \tag{5}$$

$$\langle r_{shell} \rangle = \frac{1}{N_{shell}} \sum_{r1}^{r2} r_i f(r_i) \tag{6}$$

In this definition (eq 1), $\chi(k,r_i)$ is the EXAFS signal originating from scattering from a neighbor at distance $r_i$, and $\Delta N$ denotes the number of atoms in a shell with thickness $\Delta r$. Comparing eqs 1 and 2, the latter contains more degrees of freedom and does not include an approximation about the type of the bond length distribution, such as the Gaussian distribution. The caveat, as already mentioned, is that the atomic configurations sampled by the MD simulation are a function of the force fields used to describe the simulated system and, thus, are dependent on the accuracy of the underlying force field, which may not be fully satisfactory to represent the interactions, resulting in a wrong calculation of EXAFS. An alternative to the classical MD, ab initio MD (AIMD), generally provides more accurate dynamics of systems but is limited to very small sizes of the simulated systems (tens of atoms). We propose that a spectral inversion method, such as the one relying on a machine learning algorithm described above, is a viable alternative to the forward modeling methods.

**Neural Networks.** Artificial neural networks (ANNs) have been applied in materials science to solve inverse spectral problems, such as studying structure descriptors from X-ray absorption spectroscopy[60−62] to help discover new materials,[63−67] and studying structure−property relationships.[68−72] Using NNs, we have obtained the pair distribution function $(g_\rho(r))$ for monometallic and bimetallic systems, relying on MD and MD-EXAFS simulations to generate the training set for the ANN.[58,73,74] That method is inherently problematic for solving the problem of metals in molten salts, particularly actinides, which is the focus of this article, due to the intrinsic difficulty of first-principle calculations and classical MD simulations, to tackle the complexity of co-existing, disordered coordination states of metal complexes in molten salts. Therefore, an alternative method, such as ONNE ("objectively trained NN-EXAFS") developed by us earlier,[24] is an attractive tool for creating a theoretical training set for extracting the pair distribution function information for the nearest coordination shells of U in molten $UF_4$.

**ONNE Method.** ONNE is used to invert the EXAFS to $g_\rho(r)$. Rather than employing MD to generate training data, this approach uses an algorithm to create local structures based on a combination of simple Gaussian functions describing pair distributions.[24] The method can generate training structures from any combination of bond length distributions, including partial (absorber−scatterer-specific) bond length distributions from coordination shells beyond the first nearest neighbors. This approach is the logical choice for analyzing highly disordered multi-atom bonding environments and does not require MD or AIMD data. In fact, the only use of MD or AIMD data (if available) is for the purpose of demonstration that the inversion of the absorption spectra results to $g_\rho(r)$ is done correctly (because the "ground truth" $g_\rho(r)$ is available from MD/AIMD simulations for comparison with the predicted one). The proof-of-principle work reporting on the ONNE was demonstrated for the Ni−Cl complexes in $ZnCl_2$−KCl molten salt mixture modeled by AIMD.[24] There was in that particular case no benefit of applying the ONNE method to the experimental data in ref 24—because the quality of reproduction of experiment by theory was very high, and no unique results could be obtained by ONNE compared to what is already available from AIMD simulations.

For actinides, an additional challenge for the AIMD and semi-classical approaches comes from the complex nature of $[Rn]5f^n$ electron systems that can follow a more localized or delocalized (itinerant) character,[75,76] depending on the nature of the actinide materials, and conditions of temperature, pressure, etc. Thus, the latter methods are less likely to be accurate and predictive for modeling the local structure and dynamics. The ONNE method stands out as uniquely applicable for extracting the $g_\rho(r)$. To apply this method on experimental measurements, one requires special data pre-treatment. We implemented data truncation for all calculations to adapt the feasible $k$-range of the experimental data. In addition, we also tuned reference energy $(E_0)$ for $UF_4$ MD-EXAFS to match it with the experimental counterpart, and applied the optimized $\Delta E = E_{0_{cal}} - E_{0_{exp}}$ to all calculations (see Figure S1 for more details). After the training and prediction, we demonstrated reversibility using EXAFS theory—reconstruction of EXAFS from predicted $g_\rho(r)$—to validate the prediction with experimental "ground truth" directly.

## IMPLEMENTATION OF ONNE METHOD AND RESULTS

This study used the ONNE method to analyze the U $L_3$ edge EXAFS spectra in $UF_4$, reported in the literature.[42] The details of ONNE implementation are in Figures S2 and S3. Here, we present the details of the training and validation of the ONNE neural network model. Training data were generated from the ONNE method to construct clusters objectively, only by specifying the necessary information on the studied system, such as the element of the center atom, the concentration of species, and the rules of atoms distributed in the system to construct $g_\rho(r)$. To illustrate the details of the ONNE method, one snapshot of the generated structures is shown in Figure 1.
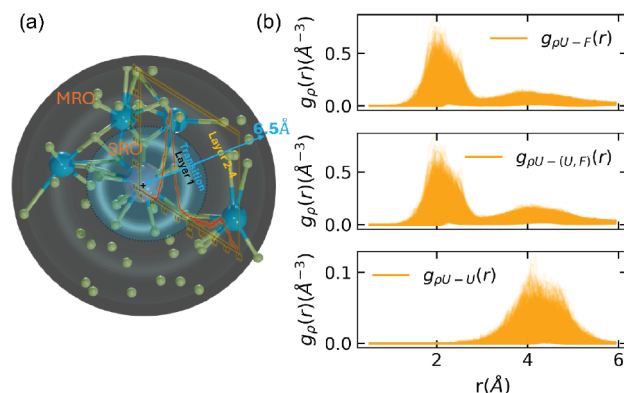


**Figure 1.** Pair distribution function and structure construction. (a) A snapshot of a structure in one $g_\rho(r)$ configuration (big blue atoms are U, and small green atoms are F). (b) Configurational average $g_\rho(r)$ for training set construction. The top $g_\rho(r)$ values considered all pairs of atoms, which we used in the neural network study. Middle and bottom considered only U−F and U−U bond distributions separately. In the PDF construction, layer 1, layer 2, the transition region, and layer 4 are all F atoms, while layer 3 contains U atoms.

In the method, one starts by defining the absorber-specific pair distribution function $g_\rho(r)$ with abstract statistical distribution functions such as a uniform distribution and Gaussian distribution. Next, atoms are sampled within the real space, adhering to the given pair distribution function constraint. This process leads to the formation of several small clusters, each exhibiting unique local structures established under the same $g_\rho(r)$ configuration but differing in their local environments. These distinct clusters are then utilized for the EXAFS calculations. In our work, we generated 100 structures for each $g_\rho(r)$ configuration. Each of our structures contained approximately 60 atoms within a radius of up to 6.5 Å from the center U atom, as shown in Figure 1a. The $g_\rho(r)$ is calculated on the structures to ensure nothing went wrong when constructing the real space models. In addition, the average of all $g_\rho(r)$ values for a given configuration is compared to the initial abstract statistical distribution function, ensuring they converge. The EXAFS spectra were calculated using the FEFF10 code.[77] In parallel to $g_\rho(r)$, the EXAFS spectra were also averaged for each configuration.

We moreover prepared a $UF_4$ MD trajectory to test our method and compare the predicted with the known (from MD) trajectory $g_\rho(r)$. The time-spatial averaged $g_\rho(r)$ and EXAFS was calculated by averaging 30 000 uranium local environments in the MD trajectory. In addition, molten $UF_4$ experimental data from ref 42 was prepared for predicting the

unknown $g_\rho(r)$. The difference in the reference energy $E_0$ of EXAFS between simulations and experimental data poses challenges in comparing the EXAFS spectra. To minimize the artifacts introduced by $E_0$, we added a $\Delta E_0$ correction to all calculations, which acts on EXAFS to redistribute $k$ grids and correct the phase and intensity. We found the optimized $\Delta E_0$ = 5.92 eV using an optimization algorithm discussed in the Supporting Information. We also explored the use of a reduction factor $S_0^2 = 0.71$ applied to simulations to address the intensity differences between simulated and experimental spectra. Further elaboration on this can be found in Sections S3 and S4, Figure S6 and Table S1).

For data construction, we used the $k^3$-weighted EXAFS and cut the $k$-range smoothly with the Hanning window to minimize the influence of the low-$k$ and high-$k$ regions. We prepared two sets of EXAFS data, employing two $k$ ranges: [2,8 $\text{Å}^{-1}$] and [2,10 $\text{Å}^{-1}$] and train separately, to illustrate the quality of predictions regarding the length of $k$ ranges. For training data, we introduced noise with a maximum level of 0.1 $\text{Å}^{-3}$ in the spectra to the model to improve the generalization of convolutional neural network (CNN) model, and used un-noised data to validate the training step. Figure 2 illustrates one
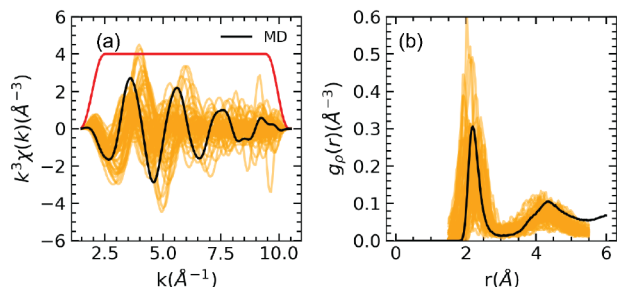


**Figure 2.** One batch of "clean" data for validation of our method. The calculated EXAFS (a) for the corresponding PDF (b) is shown by black curves. Each EXAFS spectrum and PDF are averages from 100 different structures. A Hanning window function (red curve) with the "window sills" ($dk$) of 1 $\text{Å}^{-1}$ was used to truncate theoretical and experimental EXAFS data.

batch of unknown data for the validation step in the training process. More information related to training and the CNN model used is presented in the Supporting Information.

After training, the neural network model was tested using MD-EXAFS data. To obtain the uncertainty from the model, we ran the same model 10 times, saved checkpoints of each

model, and considered the fluctuation of the predictions. The predicted results are shown in Figure 3a,b). The agreement between the prediction and the "ground truth" (MD-EXAFS data) is very good in the first peak (U–F) region. The weak feature at around 1.75 $\text{Å}^{-1}$ is smaller than the uncertainty (shown by fuzzy curves in Figure 3) due to the variation in NN hyper-parameters. The second peak, characterizing the U–U and second shell U–F pairs, shows that the NN-EXAFS method, although qualitatively replicating the trend, under-estimates the $g_\rho(r)$ intensity in that region. Nevertheless, the prediction using the $k$-range [2,10 $\text{Å}^{-1}$] outperforms the one derived from the shorter range. It offers an explanation that employing longer $k$-range can result in a better approximation to the higher shell.

The coordination numbers were calculated by integrating the predicted PDF in the 1.8–3 Å range. The predicted result of the experimental data using a $k$-range up to 10 $\text{Å}^{-1}$ is shown in Figure 3c. From experimental prediction, the coordination number was obtained to be 7.4 ± 0.7 (we used the cutoff distance up to 3 Å), versus 8.0 ± 0.6 from the MD prediction using the model training with $k$-range from 1.5 to 10 $\text{Å}^{-1}$. We also calculated the bond length ($r$) from MD simulations and the NN-EXAFS predictions, as summarized in Table 1. Most

**Table 1. Comparison of Coordination Numbers and First-Shell Bond Lengths Obtained by Different Methods**

|  | MD | MD-EXAFS ONNE prediction $k\epsilon[1.5,10\ \text{Å}^{-1}]$ | experimental EXAFS ONNE prediction $k\epsilon[1.5,10\ \text{Å}^{-1}]$ |
|---|---|---|---|
| CN | 7.9 | 8.0(6) | 7.4(7) |
| $r$ (Å) | 2.31 | 2.34(1) | 2.38(2) |

notably, the observed increases in bond length calculated using the experimental data compared to the MD predictions (Table 1) are consistent with the findings in ref 42. The relative reduction in the coordination number in the experimental data compared to that obtained in MD simulation is consistent with the trends in the first shell peak intensity visible in Figure 3c.

**Reversibility Test.** We furthermore traced the predicted PDF back to EXAFS—like functions using eqs 2 and 3 to validate the reversibility of the EXAFS spectra. The $f_i(k)$, $\lambda(k)$, and $\delta(k)$, the scattering path-dependent functions, were calculated using FEFF10. This work only used the parameters from the first single scattering path. The experimental data were employed for comparison after back Fourier transform solely on the first shell (refer to Figure S7). The results are
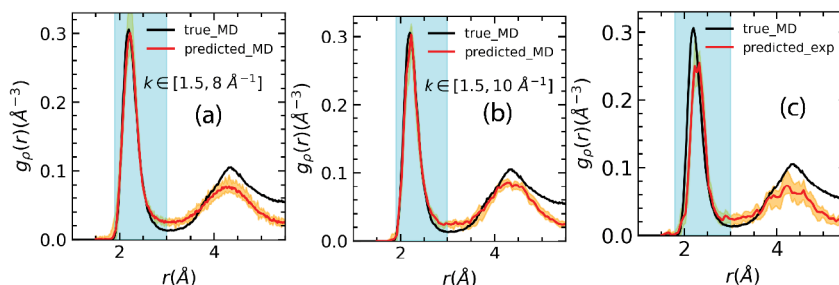


**Figure 3.** Predictions from ONNE model adapted for the relatively short $k$-range [1.5,8 $\text{Å}^{-1}$] (a) and for long $k$-range [1.5,10 $\text{Å}^{-1}$] (b) on the MD-EXAFS data and on the experimental data (c). The PDF calculated by MD is shown as a black line for comparison. The improvement of the extraction of the PDF with ONNE as the $k$-range increases is evident in the second shell region (b vs a). The orange region represents the uncertainty obtained by running the model 10 times. The blue range corresponds to the first shell, which is utilized for calculating the coordination number (CN) and bond length ($r$), listed in Table 1.

shown in Figure 4. The calculated spectrum fits very well with the experimental data. However, for MD-EXAFS-extracted
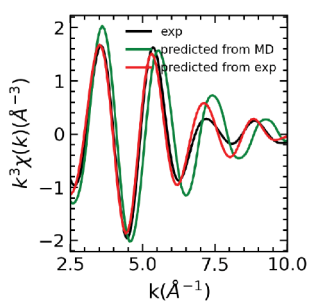


**Figure 4.** Reconstruction of EXAFS from the predicted PDF. The red line represents the average of 10 predictions. The black line illustrates the experimental data after back Fourier transform (see Figure S7) utilizing the first shell.

$g_\rho(r)$, the simulation has a phase shift because of the smaller bond length distance in MD compared to the experiment. This comparison, therefore, validates our neural network—assisted inversion of the EXAFS spectrum and its mapping onto the PDF because this process is demonstrated to be reversible: the EXAFS reconstructed from a prediction of the PDF matches well with the experimental spectrum, as illustrated in Figure 4. Moreover, the reconstruction shows a correction in phase compared to the reconstruction from the MD-EXAFS result.

## DISCUSSION

In this work, we constructed a machine-learning workflow to decode $g_\rho(r)$ from EXAFS, and for the first time, we used experimental data as a source for prediction. We also provided a validation approach to check the reversibility of our predictions, as discussed earlier. The prediction of $g_\rho(r)$ from MD-EXAFS overlaps the ground truth of the first peak and provides evidence that the neural network method can capture the features of the first coordination shell. The prediction from experimental data shows a decrease in the intensity and a shift to higher radial distances of the first peak (e.g., U—F), providing longer bond length distance than MD results. Subsequently, we reconstructed EXAFS from predicted $g_\rho(r)$. In this step, we first validated our method by checking the reversibility of MD-EXAFS (see result in the Supporting Information), and demonstrated that the reconstruction matches well with the MD-EXAFS ground truth. After this validation, we performed the same process for experimental data, showing that the reconstructed EXAFS is much closer to ground truth and could correct the existing phase shift in MD-EXAFS. Compared to the traditional EXAFS fitting method, the proposed objective training method is more robust without any prior hypothesis on $g(r)$, and the result can be self-validated by checking the reversibility with experimental data.

## CONCLUSIONS AND OUTLOOK

The proposed objective method opens a new avenue to study local coordination environments for highly disordered and amorphous materials, which are difficult to understand based on the limitations of experimental approaches and computational simulations. For example, molecular dynamics may fail for complex systems if for instance an inaccurate force field is used, if MD suffers insufficient sampling, and omits new environments in the studied system.[72] Experimental ap-

proaches, such as EXAFS, based on the strong Gaussian approximation, can result in a wrong estimation of the descriptors. In those cases, the objective method shows a high potential to study the local structure correctly. The potential of this method is not limited to $UF_4$ and other molten salts, and can be expanded to other fields, such as the $Co^{2+}$ ions doping in a nanostructural glass, where different Co local geometry can result in optical property changes,[78] complex concentrated alloys, where EXAFS fails to capture local structure,[79] and some biological catalysts, such as enzymes with specific metal active sites.[80−82] However, the current method still needs improvement, such as by improving the speed and efficiency of objective structure generation.

In general, to understand the local structure of a complex system, such as the molten $UF_4$ system, different techniques are often needed to reach a convincing conclusion. The extracted coordination numbers can vary quite strongly based on different techniques.[83] For reference, a structural refinement of crystalline $UCl_3$ by diffraction methods resulted in the coordination of U−Cl of 8[84] or 9,[85] but experimental X-ray diffraction and neutron diffraction, as well as MD and AIMD data in the melt, indicated coordination numbers as low as 6 or 7.05, and as high as 8.1, depending on the method of investigation,[85] thereby demonstrating again the challenge in the determination of the "ground truth." In the case of $UF_4$, it is worth pointing out that the results obtained herein are in line with another discrepancy noted in the literature. The density predictions by MD using the PIM force fields, are higher than the experimental correlations (see, e.g., Figure 11 in Ref. 41). The density is directly linked to the local structure, and the higher density matches the lower radial distances and higher CNs observed in the $g_\rho(r)$ obtained by MD, and predicted by our method using MD-EXAFS data.

## ASSOCIATED CONTENT

### ⓢ Supporting Information

The Supporting Information is available free of charge at https://pubs.acs.org/doi/10.1021/acs.jpcc.4c01898.

> Data preparation, neural network architecture, and determination of the EXAFS passive electron reduction factor; additional Supporting Information (Python codes, training data set) is placed at Zenodo: 10.5281/zenodo.10676964; the codes are also available at the Github repository: https://github.com/kaifengZheng/CNN_EXAFS_PDF.git (PDF)

## AUTHOR INFORMATION

### Corresponding Author

**Anatoly I. Frenkel** − *Department of Materials Science and Chemical Engineering, Stony Brook University, Stony Brook, New York 11794, United States; Chemistry Division, Brookhaven National Laboratory, Upton, New York 11973, United States;* ⓞ orcid.org/0000-0002-5451-1207; Email: Anatoly.Frenkel@stonybrook.edu

### Authors

**Kaifeng Zheng** − *Department of Materials Science and Chemical Engineering, Stony Brook University, Stony Brook, New York 11794, United States*

**Nicholas Marcella** − *Department of Chemistry, University of Illinois, Urbana, Illinois 61801, United States*

**Anna L. Smith** − *Department of Radiation Science and Technology, Delft University of Technology, Delft 2629 JB, The Netherlands;* orcid.org/0000-0002-0355-5859

## ■ ACKNOWLEDGMENTS

## ■ REFERENCES

(1) Kolobov, A. V.; Fons, P.; Frenkel, A. I.; Ankudinov, A. L.; Tominaga, J.; Uruga, T. Understanding the Phase-Change Mechanism of Rewritable Optical Media. *Nat. Mater.* 2004, 3 (10), 703−8708.

(2) Cai, Z.; Zhou, D.; Wang, M.; Bak, S. M.; Wu, Y.; Wu, Z.; Tian, Y.; Xiong, X.; Li, Y.; Liu, W.; et al. Introducing Fe(2+) into Nickel-Iron Layered Double Hydroxide: Local Structure Modulated Water Oxidation Activity. *Angew. Chem., Int. Ed.* 2018, 57 (30), 9392−9396.

(3) Halder, A.; Lenardi, C.; Timoshenko, J.; Mravak, A.; Yang, B.; Kolipaka, L. K.; Piazzoni, C.; Seifert, S.; Bonačić-Koutecký, V.; Frenkel, A. I.; et al. CO2Methanation on Cu-Cluster Decorated Zirconia Supports with Different Morphology: A Combined Experimental In Situ GIXANES/GISAXS, Ex Situ XPS and Theoretical DFT Study. *ACS Catal.* 2021, 11 (10), 6210−6224.

(4) Hinokuma, S.; Kawabata, Y.; Matsuki, S.; Shimanoe, H.; Kiritoshi, S.; Machida, M. Local Structures and Catalytic Ammonia Combustion Properties of Copper Oxides and Silver Supported on Aluminum Oxides. *J. Phys. Chem. C* 2017, 121 (8), 4188−4196.

(5) Jakub, Z.; Hulva, J.; Meier, M.; Bliem, R.; Kraushofer, F.; Setvin, M.; Schmid, M.; Diebold, U.; Franchini, C.; Parkinson, G. S. Local Structure and Coordination Define Adsorption in a Model Ir(1)/Fe(3) O(4) Single-Atom Catalyst. *Angew. Chem., Int. Ed.* 2019, 58 (39), 13961−13968.

(6) Wang, H.; Kottwitz, M.; Rui, N.; Senanayake, S. D.; Marinkovic, N.; Li, Y.; Nuzzo, R. G.; Frenkel, A. I. Aliovalent Doping of CeO(2) Improves the Stability of Atomically Dispersed Pt. *ACS Appl. Mater. Interfaces* 2021, 13 (44), 52736−52742.

(7) Yalcin, O.; Molinari Erwin, J. E.; Gerceker, D.; Onal, I.; Wachs, I. E. Role of Local Structure on Catalytic Reactivity: Comparison of Methanol Oxidation by Aqueous Bioinorganic Enzyme Mimic (Vanadium Haloperoxidase) and Vanadia-Based Heterogeneous Catalyst (Supported VO4/SiO2). *ACS Catal.* 2020, 10 (2), 1566−1574.

(8) Kottwitz, M.; Li, Y.; Palomino, R. M.; Liu, Z.; Wang, G.; Wu, Q.; Huang, J.; Timoshenko, J.; Senanayake, S. D.; Balasubramanian, M.; et al. Local Structure and Electronic State of Atomically Dispersed Pt Supported on Nanosized CeO2. *ACS Catal.* 2019, 9 (9), 8738−8748.

(9) Vogt, C.; Meirer, F.; Monai, M.; Groeneveld, E.; Ferri, D.; van Santen, R. A.; Nachtegaal, M.; Unocic, R. R.; Frenkel, A. I.; Weckhuysen, B. M. Dynamic Restructuring of Supported Metal Nanoparticles and its Implications for Structure Insensitive Catalysis. *Nat. Commun.* 2021, 12 (1), 7096.

(10) Li, Y.; Kottwitz, M.; Vincent, J. L.; Enright, M. J.; Liu, Z.; Zhang, L.; Huang, J.; Senanayake, S. D.; Yang, W. D.; Crozier, P. A.; et al. Dynamic Structure of Active Sites in Ceria-Supported Pt Catalysts for the Water Gas Shift Reaction. *Nat. Commun.* 2021, 12 (1), 914.

(11) Zhang, S.; Tang, Y.; Nguyen, L.; Zhao, Y.-F.; Wu, Z.; Goh, T.-W.; Liu, J. J.; Li, Y.; Zhu, T.; Huang, W.; et al. Catalysis on Singly Dispersed Rh Atoms Anchored on an Inert Support. *ACS Catal.* 2018, 8 (1), 110−121.

(12) Zhang, F.; Liu, Z.; Zhang, S.; Akter, N.; Palomino, R. M.; Vovchok, D.; Orozco, I.; Salazar, D.; Rodriguez, J. A.; Llorca, J.; et al. In Situ Elucidation of the Active State of Co−CeOx Catalysts in the Dry Reforming of Methane: The Important Role of the Reducible Oxide Support and Interactions with Cobalt. *ACS Catal.* 2018, 8 (4), 3550−3560.

(13) Erickson, E. M.; Thorum, M. S.; Vasić, R.; Marinković, N. S.; Frenkel, A. I.; Gewirth, A. A.; Nuzzo, R. G. In Situ Electrochemical X-ray Absorption Spectroscopy of Oxygen Reduction Electrocatalysis with High Oxygen Flux. *J. Am. Chem. Soc.* 2012, 134 (1), 197−200.

(14) Wolf, T.; Kumar, S.; Singh, H.; Chakrabarty, T.; Aussenac, F.; Frenkel, A. I.; Major, D. T.; Leskes, M. Endogenous Dynamic Nuclear Polarization for Natural Abundance 17O and Lithium NMR in the Bulk of Inorganic Solids. *J. Am. Chem. Soc.* 2019, 141 (1), 451−462.

(15) Breuer, O.; Chakraborty, A.; Liu, J.; Kravchuk, T.; Burstein, L.; Grinblat, J.; Kauffman, Y.; Gladkih, A.; Nayak, P.; Tsubery, M.; et al. Understanding the Role of Minor Molybdenum Doping in LiNi0.5Co0.2Mn0.3O2 Electrodes: from Structural and Surface Analyses and Theoretical Modeling to Practical Electrochemical Cells. *ACS Appl. Mater. Interfaces* 2018, 10 (35), 29608−29621.

(16) Piovano, A.; Agostini, G.; Frenkel, A. I.; Bertier, T.; Prestipino, C.; Ceretti, M.; Paulus, W.; Lamberti, C. Time Resolved in Situ XAFS Study of the Electrochemical Oxygen Intercalation in SrFeO2.5 Brownmillerite Structure: Comparison with the Homologous SrCoO2.5 System. *J. Phys. Chem. C* 2011, 115 (4), 1311−1322.

(17) Clausen, B. S.; Nørskov, J. K. Asymmetric Pair Distribution Functions in Catalysts. *Top. Catal.* 2000, 10, 221−230.

(18) Li, J.; Li, Y.; Routh, P. K.; Makagon, E.; Lubomirsky, I.; Frenkel, A. I. Comparative Analysis of XANES and EXAFS for Local Structural Characterization of Disordered Metal Oxides. *J. Synchrotron Radiat.* 2021, 28, 1511−1517.

(19) Vila, F.; Rehr, J. J.; Kas, J.; Nuzzo, R. G.; Frenkel, A. I. Dynamic Structure in Supported Pt Nanoclusters: Real-Time Density Functional Theory and X-ray Spectroscopy Simulations. *Phys. Rev. B* 2008, 78 (12), 121404.

(20) D'Angelo, P.; Di Nola, A.; Filipponi, A.; Pavel, N. V.; Roccatano, D. An Extended X-ray Absorption Fine Structure Study of Aqueous Solutions by Employing Molecular Dynamics Simulations. *J. Chem. Phys.* 1994, 100 (2), 985−994.

(21) Palmer, B. J.; Pfund, D. M.; Fulton, J. L. Direct Modeling of EXAFS Spectra from Molecular Dynamics Simulations. *J. Phys. Chem.* 1996, 100 (32), 13393−13398.

(22) Gill, S. K.; Huang, J.; Mausz, J.; Gakhar, R.; Roy, S.; Vila, F.; Topsakal, M.; Phillips, W. C.; Layne, B.; Mahurin, S.; et al. Connections between the Speciation and Solubility of Ni(II) and Co(II) in Molten ZnCl2. *J. Phys. Chem. B* 2020, 124 (7), 1253−1258.

(23) Anderson, R. M.; Zhang, L.; Loussaert, J. A.; Frenkel, A. I.; Henkelman, G.; Crooks, R. M. An Experimental and Theoretical Investigation of the Inversion of Pd@Pt Core@Shell Dendrimer-Encapsulated Nanoparticles. *ACS Nano* 2013, 7 (10), 9345−9353.

(24) Marcella, N.; Lam, S.; Bryantsev, V.; Roy, S.; Frenkel, A. I. Neural Network -Based Analysis of Multimodal Bond Distributions Using their EXAFS Spectra. *Phys. Rev. B* 2024, 109, 104201.

(25) Dupont, J. From Molten Salts to Ionic Liquids: A ″Nano″ Journey. *Acc. Chem. Res.* 2011, 44 (11), 1223−1231.

(26) Abramo, M. C.; Caccamo, C.; Pizzimenti, G.; Parrinello, M.; Tosi, M. P. Ionic Radii and Diffraction Patterns of Molten Alkali Halides. *J. Chem. Phys.* 1978, 68 (6), 2889−2895.

(27) Takahashi, S.; Muneta, T.; Koura, N.; Ohno, H. Structural Analysis of the Molten Salt 50 mol% AlCl3−50 mol% NaCl by X-ray Diffraction. *J. Chem. Soc., Faraday Trans.* 1985, 2 (81), 1107−1115.

(28) Wasse, J. C.; Salmon, P. S. Structure of Molten Lanthanum and Cerium Tri-Halides by the Method of Isomorphic Substitution in Neutron Diffraction. *J. Phys.: Condens. Matter* **1999**, *11*, 1381−1396.

(29) Adya, A. K.; Takagi, R.; Gaune-Escard, M. Unrevalling the Internal Complexities of Molten Salts. *Z. Naturforsch., A* **1998**, *53*, 1037−1048.

(30) Okamoto, Y.; Hayashi, H.; Ogawa, T. X-ray Diffraction Analysis of Molten Trivalent Halides. *Jpn. J. Appl. Phys.* **1999**, *38* (1), 156−159.

(31) Brooker, M. H.; Berg, R. W.; von Barner, J. H.; Bjerrum, N. J. Raman Study of the Hexafluoroaluminate Ion in Solid and Molten FLINAK. *Inorg. Chem.* **2000**, *39* (16), 3682−3689.

(32) Ma, Y.; Yamamoto, T.; Yasuda, K.; Nohira, T. Raman Analysis and Electrochemical Reduction of Silicate Ions in Molten NaCl−CaCl$_2$. *J. Electrochem. Soc.* **2021**, *168* (4), 046515.

(33) Raptis, C.; Mitchell, E. W. Raman scattering from molten Li and Rb halides. *J. Phys. C: Solid State Phys.* **1987**, *20*, 4513−4528.

(34) Roy, S.; Brehm, M.; Sharma, S.; Wu, F.; Maltsev, D. S.; Halstenberg, P.; Gallington, L. C.; Mahurin, S. M.; Dai, S.; Ivanov, A. S.; et al. Unraveling Local Structure of Molten Salts via X-ray Scattering, Raman Spectroscopy, and Ab Initio Molecular Dynamics. *J. Phys. Chem. B* **2021**, *125*, 5971−5982.

(35) Auguste, F.; Tkatcheva, O.; Mediaas, H.; Østvold, T.; Gilbert, B. The Dissociation of Fluoroaluminates in FLINAK and CsF-KF Molten Mixtures: ARaman Spectroscopic and Solubility Study. *Inorg. Chem.* **2003**, *42*, 6338−6344.

(36) Li, H.; Lu, K.; Wu, Z.; Jun, D. EXAFS Studies of Molten ZnCl$_2$, RbCl and Rb$_2$ZnCl$_4$. *J. Phys.: Condens. Matter* **1994**, *6*, 3629−3640.

(37) Hardacre, C. Application of EXAFS to Molten Salts and Ionic Liquid Technology. *Annu. Rev. Mater. Res.* **2005**, *35*, 29−49.

(38) Okamoto, Y.; Shiwaku, H.; Yaita, T.; Suzuki, S.; Gaune-Escard, M. High-Energy EXAFS Study of Molten GdCl3 Systems. *J. Mol. Liq.* **2013**, *187*, 94−98.

(39) Li, B.; Jones, Z. R.; Eiroa-Lledo, C.; Knope, K. E.; Mocko, V.; Stein, B. W.; Wacker, J. N.; Kozimor, S. A.; Batista, E. R.; Yang, P. Structure and Dynamics of NaCl/KCl/CaCl2-EnCln (n = 2, 3, Molten Salts. *Inorg. Chem.* **2023**, *62*, 10528−10538.

(40) Roy, S.; Liu, Y.; Topsakal, M.; Dias, E.; Gakhar, R.; Phillips, W. C.; Wishart, J. F.; Leshchev, D.; Halstenberg, P.; Dai, S.; et al. A Holistic Approach for Elucidating Local Structure, Dynamics, and Speciation in Molten Salts with High Structural Disorder. *J. Am. Chem. Soc.* **2021**, *143*, 15298−15308.

(41) Ocádiz-Flores, J. A.; Gheribi, A. E.; Vlieland, J.; Dardenne, K.; Rothe, J.; Konings, R. J. M.; Smith, A. L. New Insights and Coupled Modelling of the Structural and Thermodynamic Properties of the LiF-UF4 System. *J. Mol. Liq.* **2021**, *331*, 115820.

(42) Ocadiz-Flores, J. A.; Gheribi, A. E.; Vlieland, J.; de Haas, D.; Dardenne, K.; Rothe, J.; Konings, R. J. M.; Smith, A. L. Examination of the Short-Range Structure of Molten Salts: ThF$_4$, UF$_4$, and Related Alkali Actinide Fluoride Systems. *Phys. Chem. Chem. Phys.* **2021**, *23*, 11091−11103.

(43) Bessada, C.; Zanghi, D.; Salanne, M.; Gil-Martin, A.; Gibilaro, M.; Chamelot, P.; Massot, L.; Nezu, A.; Matsuura, H. Investigation of ionic local structure in molten salt fast reactor LiF-ThF$_4$-UF$_4$ fuel by EXAFS experiments and molecule dynamics simulations. *J. Mol. Liq.* **2020**, *307*, 112927.

(44) Kompch, A.; Sahu, A.; Notthoff, C.; Ott, F.; Norris, D. J.; Winterer, M. Localization of Ag Dopant Atoms in CdSe Nanocrystals by Reverse Monte Carlo Analysis of EXAFS Spectra. *J. Phys. Chem. C* **2015**, *119*, 18762−18772.

(45) Timoshenko, J.; Anspoks, A.; Kalinko, A.; Kuzmin, A. Local Structure of Copper Nitride Revealed by EXAFS Spectroscopy and a Reverse Monte Carlo/Evolutionary Algorithm Approach. *Phys. Scr.* **2016**, *91*, 054003.

(46) Timoshenko, J.; Anspoks, A.; Kalinko, A.; Kuzmin, A. Local Structure of Cobalt Tungstate Revealed by EXAFS Spectroscopy and Reverse Monte Carlo/Evolutionary Algorithm Simulations. *Z. Phys. Chem.* **2016**, *230* (4), 551−568.

(47) Timoshenko, J.; Frenkel, A. I. Probing Structural Relaxation in Nanosized Catalysts by Combining EXAFS and Reverse Monte Carlo Methods. *Catal. Today* **2017**, *280*, 274−282.

(48) Timoshenko, J.; Kuzmin, A.; Purans, J. Reverse Monte Carlo Modeling of Thermal Disorder in Crystalline Materials from EXAFS Spectra. *Comput. Phys. Commun.* **2012**, *183*, 1237−1245.

(49) Gurman, S. J.; McGreevy, R. L. Reverse Monte Carlo Simulation for the Analysis of EXAFS. *J. Phys.: Condens. Matter* **1990**, *2*, 9463−9473.

(50) Di Cicco, A.; Iesari, F.; Trapananti, A.; D'Angelo, P.; Filipponi, A. Structure and Atomic Correlations in Molecular Systems Probed by XAS Reverse Monte Carlo Refinement. *J. Chem. Phys.* **2018**, *148* (9), 094307.

(51) Ershov, N. V.; Ageev, A. L.; Vasin, V. V.; Babanov, Y. A. A New Interpretation of EXAFS Spectra in Real Space II. A Comparison of the Regularization Technique with the Fourier Transformation Method. *Phys. Status Solidi B* **1981**, *108*, 103−111.

(52) Babanov, Y.; Kiryanov, S.; Sidorenko, A.; Romashev, L.; Vyalikh, D.; Molodtsov, S.; Guentherodt, G.; Ruediger, U.; Dedkov, Y.; Fonine, M.; et al. Overlapping XAFS L Spectra of 3d Metals A New Application of the Regularization Method. *Phys. Scr.* **2005**, *2005*, 194−196.

(53) Kuzmin, A.; Chaboy, J. EXAFS and XANES analysis of Oxides at the nanoscale. *IUCrJ* **2014**, *1*, 571−589.

(54) Yang, D. S.; Bunker, G. Improved R-space Resolution of EXAFS Spectra Using Combined Regularization Methods and Nonlinear Least-Squares Fitting. *Phys. Rev. B* **1996**, *54* (5), 3169.

(55) Babanov, Y. A.; Kamensky, I. Y.; Hazemann, J. L.; Calzavara, Y.; Raoux, D. Partial Pair Correlation Functions for Multicomponent Systems by EXAFS: A New Approach. *Nucl. Instrum. Methods Phys. Res., Sect. A* **2007**, *575*, 155−158.

(56) Timoshenko, J.; Lu, D.; Lin, Y.; Frenkel, A. I. Supervised Machine-Learning-Based Determination of Three-Dimensional Structure of Metallic Nanoparticles. *J. Phys. Chem. Lett.* **2017**, *8* (20), 5091−5098.

(57) Timoshenko, J.; Frenkel, A. I. Inverting" X-ray Absorption Spectra of Catalysts by Machine Learning in Search for Activity Descriptors. *ACS Catal.* **2019**, *9* (11), 10192−10211.

(58) Timoshenko, J.; Anspoks, A.; Cintins, A.; Kuzmin, A.; Purans, J.; Frenkel, A. I. Neural Network Approach for Characterizing Structural Transformations by X-Ray Absorption Fine Structure Spectroscopy. *Phys. Rev. Lett.* **2018**, *120* (22), 225502.

(59) Timoshenko, J.; Wrasman, C. J.; Luneau, M.; Shirman, T.; Cargnello, M.; Bare, S. R.; Aizenberg, J.; Friend, C. M.; Frenkel, A. I. Probing Atomic Distributions in Mono- and Bimetallic Nanoparticles by Supervised Machine Learning. *Nano Lett.* **2019**, *19* (1), 520−529.

(60) Liu, Y.; Marcella, N.; Timoshenko, J.; Halder, A.; Yang, B.; Kolipaka, L.; Pellin, M. J.; Seifert, S.; Vajda, S.; Liu, P.; et al. Mapping XANES Spectra on Structural Descriptors of Copper Oxide Clusters Using Supervised Machine Learning. *J. Chem. Phys.* **2019**, *151* (16), 164201.

(61) Timoshenko, J.; Jeon, H. S.; Sinev, I.; Haase, F. T.; Herzog, A.; Roldan Cuenya, B. Linking the Evolution of Catalytic Properties and Structural Changes in Copper-Zinc Nanocatalysts Using Operando EXAFS and Neural-Networks. *Chem. Sci.* **2020**, *11*, 3727−3736.

(62) Trejo, O.; Dadlani, A. J.; Acharya, S.; Kravec, R.; Nordlund, D.; Sarangi, R.; Prinz, F. B.; Torgersen, J.; Dasgupta, N. P. Elucidating the Evolving Atomic Structure in Atomic Layer Deposition Reactions with in Situ XANES and Machine Learning. *Chem. Mater.* **2019**, *31* (21), 8937−8947.

(63) Juan, Y.; Dai, Y.; Yang, Y.; Zhang, J. Accelerating Materials Discovery Using Machine Learning. *J. Mater. Sci. Technol.* **2021**, *79*, 178−190.

(64) Cai, J.; Chu, X.; Xu, K.; Li, H.; Wei, J. Machine Learning-Driven New Material Discovery. *Nanoscale Adv.* **2020**, *2*, 3115−3130.

(65) Liu, Y.; Zhao, T.; Ju, W.; Shi, S. Materials discovery and design using machine learning. *J. Materiomics* **2017**, *3* (3), 159−177.

(66) Schmidt, J.; Marques, M. R. G.; Botti, S.; Marques, M. A. L. Recent Advances and Applications of Machine Learning in Solid-State Materials Science. *npj Comput. Mater.* **2019**, *5* (1), 83.

(67) Hong, Y.; Hou, B.; Jiang, H.; Zhang, J. Machine Learning and Artificial Neural Network Accelerated Computational Discoveries in Materials Science. *Wiley Interdiscip. Rev.: Comput. Mol. Sci.* **2020**, *10* (3), 1450.

(68) Charest, N.; Tro, M.; Bowers, M. T.; Shea, J.-E. Latent Models of Molecular Dynamics Data: Automatic Order Parameter Generation for Peptide Fibrillization. *J. Phys. Chem. B* **2020**, *124*, 8012−8022.

(69) Pilania, G.; Wang, C.; Jiang, X.; Rajasekaran, S.; Ramprasad, R. Accelerating materials property predictions using machine learning. *Sci. Rep.* **2013**, *3* (1), 2810.

(70) Zhou, Q.; Lu, S.; Wu, Y.; Wang, J. Property-oriented Material Design Based on a Data-Driven Machine Learning Technique. *J. Phys. Chem. Lett.* **2020**, *11*, 3920−3927.

(71) Tavazza, F.; DeCost, B.; Choudhary, K. Uncertainty Prediction for Machine Learning Models of Material Properties. *ACS Omega* **2021**, *6*, 32431−32440.

(72) Moosavi, S. M.; Jablonka, K. M.; Smit, B. The Role of Machine Learning in the Understanding and Design of Materials. *J. Am. Chem. Soc.* **2020**, *142*, 20273−20287.

(73) Timoshenko, J.; Roldan Cuenya, B. In Situ/Operando Electrocatalyst Characterization by X-ray Absorption Spectroscopy. *Chem. Rev.* **2021**, *121*, 882−961.

(74) Boubnov, A.; Timoshenko, J.; Wrasman, C. J.; Hoffman, A. S.; Cargnello, M.; Frenkel, A. I.; Bare, S. R. Insight into Restructuring of Pd-Au Nanoparticles Using EXAFS. *Radiat. Phys. Chem.* **2020**, *175*, 108304.

(75) Caciuffo, R.; Lander, G. H.; van der Laan, G. Synchrotron Radiation Techniques and their Application to Actinide Materials. *Rev. Mod. Phys.* **2023**, *95* (1), 015001.

(76) Andersson, D. A.; Beeler, B. W. Ab initio molecular dynamics (AIMD) simulations of NaCl, UCl3 and NaCl-UCl3 molten salts. *J. Nucl. Mater.* **2022**, *568*, 153836.

(77) Kas, J. J.; Vila, F. D.; Pemmaraju, C. D.; Tan, T. D.; Rehr, J. J. Advanced Calculations of X-ray Spectroscopies with FEFF10 and Corvus. *J. Synchrotron Radiat.* **2021**, *28*, 1801−1810.

(78) Lin, L.; Wang, Y.; Lan, L.; Chen, J.; Lv, S.; Zhao, Y.; Yu, H.; Hao, J.; Zhang, Q.; Yang, Z.; et al. Coordination Geometry Engineering in a Doped Disordered Matrix for Tunable Optical Response. *J. Phys. Chem. C* **2019**, *123*, 29343−29352.

(79) Joress, H.; Ravel, B.; Anber, E.; Hollenbach, J.; Sur, D.; Hattrick-Simpers, J.; Taheri, M. L.; DeCost, B. Why is EXAFS for complex concentrated alloys so hard? Challenges and opportunities for measuring ordering with X-ray absorption spectroscopy. *Matter* **2023**, *6* (11), 3763−3781.

(80) Eggers-Borkenstetn, P.; Priggemeyer, S.; Krebs, B.; Henkel, G.; Simons, U.; Pettiff, R. F.; Nolting, H.-F.; Hermess, C. Extended X-ray Absorption Fine Structure (EXAFS) Investigations of Model Compounds for Zinc Enzymes. *Eur. J. Biochem.* **1989**, *186* (3), 667−675.

(81) Ji, S.; Jiang, B.; Hao, H.; Chen, Y.; Dong, J.; Mao, Y.; Zhang, Z.; Gao, R.; Chen, W.; Zhang, R.; et al. Matching the Kinetics of Natural Enzymes with a Single-Atom Iron Nanozyme. *Nat. Catal.* **2021**, *4*, 407−417.

(82) Muller, A.; Erkens, A.; Schneider, K.; Muller, A.; Nolting, H.-F.; Sole, V. A.; Henkel, G. NADH-Induced Changes of the Nickel Coordination within the Active Site of the Soluble Hydrogenase from Alcaligenes eutrophus: XAFS Investigations on Three States Distinguishable by EPR Spectroscopy. *Angew. Chem., Int. Ed.* **1997**, *36* (16), 1747−1750.

(83) Smith, A. L. Structure-Property Relationships in Actinide Containing Molten Salts - A Review: Understanding and Modeling the Chemistry of Nuclear Fuel Salts. *J. Mol. Liq.* **2022**, *360*, 119426.

(84) Okamoto, Y.; Madden, P. A.; Minato, K. X-ray Diffraction and Molecular Dynamics Simulation Studies of Molten Uranium Chloride. *J. Nucl. Mater.* **2005**, *344*, 109−114.

(85) Smith, A. L. Structure-Property Relationships in Actinide Containing Molten Salts − A Review: Understanding and Modelling the Chemistry of Nuclear Fuel Salts. *J. Mol. Liq.* **2022**, *360*, 119426.